www.czasopisma.pan.pl PAN POLSKA AKADEMIA NAUK www.journals.pan.pl

Arch. Metall. Mater. **68** (2023), 3, 839-849

DOI: https://doi.org/10.24425/amm.2023.145446

JIALUN WU[1], MIN XIA[1*], JUNFENG WANG[1], CHANGCHUN GE[1]

EFFECT OF ELECTRODE INDUCTION MELTING GAS ATOMIZATION PROCESS ON FINE POWDER YIELDS: CONTINUOUS METAL MELT FLOW

Electrode induction melting gas atomization (EIGA) is a newly developed method for preparing ultra-clean metal powders, and is a completely crucible-free melting and atomization process. Based on conducted several atomization experiments, we found that the fine powder yields obtained during the EIGA process were greatly affected by the status of metal melt flow. While, continuous metal melt flow was beneficial for the yield of fine powders, it was in conflict with the principle described for the vacuum induction melting inert gas atomization (VIGA) process. To understand the critical role of continuous metal melt flow in the EIGA process, a computational fluid dynamics (CFD) approach was developed to simulate the gas atomization process. The D50 particle size of powder prepared by atomization under continuous liquid metal flow was about 70 μm, while that obtained by atomization under non-continuous liquid metal flow was about 100 μm. The diameter distribution results of numerical simulations agreed well with the experimental measurements, which demonstrated the accuracy of our simulation method. This study provides theoretical support for understanding the critical role of continuous metal melt flow and improving fine powder yields in the EIGA process.

PACS: 02.60.Cb; 43.28.Py; 41.20.Gz; 81.20.Ev

Keywords: gas atomization; powder metallurgy; numerical simulation; computational fluid dynamics

1. Introduction

In recent years, the application of metal powders has increased considerably, and the production of high-quality pure metal powders is an important process in the fields of aerospace, powder metallurgy, and additive manufacturing. Zhu summarized methods of preparing metal powders, including mechanical crushing, ball-milling, gas atomization, electrolysis, and oxidation [1]. Si proposed using the gas-atomization method to prepare superfine powders and found that the benefits of gas-atomized powders arise from better spherical shape and lower surface oxygen content, particularly when the atomization is conducted under an inert gas atmosphere or under vacuum [2]. In recent years, many studies have been conducted on vacuum induction melting inert gas atomization (VIGA), which can produce ultrafine powders with low oxygen content [3]. However, since that active metals and alloys easily react with the ceramic materials of crucibles and delivery tubes under melting conditions, which results in the presence of certain amounts of non-metallic inclusions in the metal powder, Qiu has also demonstrated the occurrence of inclusions and defects in Ni-based superalloys produced by powder, which may seriously affect the performance of the produced superalloy components, and even cause safety incidents [4]. In the EIGA method, the melt flow is not in contact with refractories such as crucible ceramics. Bojarevics proved that the free-fall nozzle uesd in EIGA was crucible-free, and Zheng mentioned that the EIGA method is often used to prepare ultra-clean metal powders which tend to react with crucible materials [5-7].

The EIGA method is associated with two major problems. The first is the optimal design of the free-flow nozzles, and the second is the control of induction melting of the metal electrode. More specifically, the former concerns the process of atomization, while the latter refers to the control of the continuous metal liquid flow by regulating the induction coil and power parameters. Özbilen studied the influence of liquid metal properties on the particle size of gas-atomized powders, and Ting studied the close-coupled gas atomization nozzle by numerical simulation; both research groups all proved that non-continuous metal flow improves fine powder yields in VIGA [8,9]. However, it was found that non-continuous metal fluid using free-fall nozzles could reduce the productivity of fine powders in the EIGA

[1] UNIVERSITY OF SCIENCE & TECHNOLOGY BEIJING, INSTITUTE OF POWDER METALLURGY AND ADVANCED CERAMICS, BEIJING 100083, CHINA

* Corresponding author: xmdsg@ustb.edu.cn

process, and it was likely to be affected by the back-flow zone [10]. These two conclusions concerning the gas atomization process are completely opposite, and nearly no one mentioned the relationship between the condition of metal flow and the productivity of fine powders. Studies have shown that the mechanical properties of powder metallurgy parts prepared by ultrafine powder are high, and the application of continuous metal fluid might be one method to increase ultrafine powder yields [11]. Therefore, it is necessary to understand the critical role of continuous metal melt flow in the EIGA process.

Since gas atomization is a complex physical process, where a high-speed gas breaks a high-temperature fluid into small droplets in a very short time, conventional experimental methods are inadequate to characterize the entire crushing process. Therefore, a computational fluid dynamics (CFD) approach was developed to simulate the gas atomization process. For example, Xia designed a simulation of the entire gas atomization process and proved that the numerical simulation results agreed well with the experimental measurements [12]. Minghao designed the characteristics for a dual-fluid atomizer by 3D numerical simulation, and the effects of different air-flow velocities and atomizer geometry parameters on the water absorption capacity of the atomizer were also studied and revealed [13]. Motaman, Zeoli & Gu and Chen conducted numerical simulations to investigate the application and performance of close-coupled nozzles; Motaman studied different gas-jet mismatch angles on the back-stream flow in close-coupled gas atomization by numerical simulation, Zeoli & Gu studied the mechanism of droplet break-up in primary atomization, and Chen provided the details of numerical simulation for gas atomization [14-16]. According to these studies, visualization of the atomization process can be achieved by numerical simulation.

This paper aims to understand the critical role of continuous metal melt flow in the EIGA process on the yield of ultrafine powder. The simulation of melt flow and atomization was performed using the commercial CFD software FLUENT to obtain the particle size distribution of the powders using the EIGA method. This work provides theoretical support for understanding the critical role of continuous metal melt flow, and thus improving fine powder yields in EIGA.

2. Metal melt flow

2.1. Continuous and non-continuous metal melt flow in the EIGA process

To prove the rationality and necessity of this study, experiments were performed on an EIGA device. FGH4096 superalloy was selected as the metal in the experiments, and compressed argon was used as the atomization gas (Fig. 1).

The diameter of the used Ni-based superalloy rod was 55 mm, and the composition of the alloy was is listed in TABLE 1.

We found that the type of metal melt metal flow was controlled by certain process parameters, such as induction coil size and power supply [17]. The atomizing chamber was evacuated until a pressure of 5×10^{-3} Pa was reached. The atomization gas pressure was 4 MPa, and the smelting power was altered from

Fig. 1. Self-developed EIGA device; (a) EIGA device, (b) superalloy bar, (c) melting chamber

TABLE 1

Composition and content of Ni-based superalloy

Component	Ni	Co	Cr	W	Ti	Al	Mo	Ta	Nb	C	B	Zr
Content / %	46.1	21.7	13.4	4.73	3.58	3.49	2.67	1.59	1.70	0.046	0.025	0.063

48 to 37 kW until the bar was heated to 1970 K. Drop and rotation speed of the superalloy bar were controlled to obtain two different metal melt flow conditions (Fig. 2).

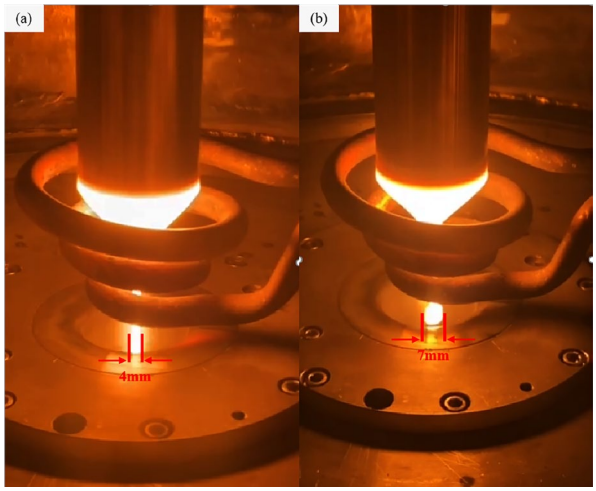

Fig. 2. Comparison between metal melt flows; (a) Continuous flow, (b) non-continuous flow

The metal melt flow in Fig. 2(a) was in a continuous state (the diameter was nearly 4 mm), while that in Fig. 2(b) was broken into droplets, and the diameter of the falling droplet was about 7 mm. Thus, the existence of the two different liquid flow states was confirmed.

SEM images of atomized powders and the comparison of the distribution of the particle diameters are shown in Fig. 3, Figs. 3(a) and (b) indicated that most of the powders were nearly spherical with only a few irregular-shaped powder particles, which verified the excellent production characteristics of the EIGA process.

However, the particle size of the powders in Fig. 3(c) obtained under continuous flow was much smaller (the yield rate of 250-mesh sieves was 53%) than that produced under non-continuous flow (the yield rate of 250-mesh sieves was 38%).

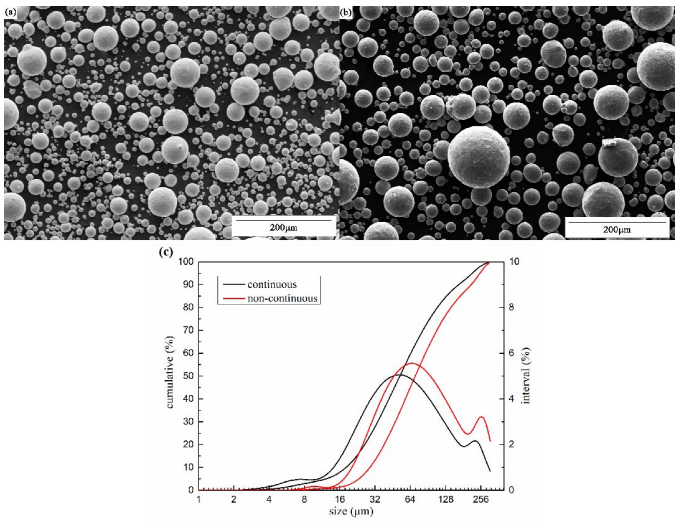

Fig. 3. SEM images of atomized powders (a, b) and distributions of powder particle size (c); (a) Continuous flow, (b) non-continuous flow

According to previous research, the particle sizes of powders produced by close-coupled nozzles were completely different from those produced here, showing that the particle sizes of the powders obtained under non-continuous flow were much smaller than those produced under continuous flow [9].

Consequently, it is necessary to investigate the conditions and mechanism of the metal fluid flow during EIGA. The subsequent chapters will demonstrate the atomization mechanism and yield analysis of continuous and discontinuous metal melt flow through numerical simulations.

2.2. Continuous metal melt flow simulation

Ideally, in EIGA, superalloy bars melt into a continuous and manageable stream of molten metal. To observe the melting flow formation process and simulate the free-fall process of liquid drop melting from the top of the alloy bar, this study uses the actual production process of a certain Ni-based superalloy as an example. The physical properties of this alloy are listed in TABLE 2.

TABLE 2

Physical properties of the Ni-based superalloy [18]

Parameter	Value	Unit
Heat capacity	720	$J \cdot kg^{-1} \cdot K^{-1}$
Thermal conductivity	29.6	$W \cdot m^{-1} \cdot K^{-1}$
Viscosity	0.05	mPa·s
Surface tension	1.84	$mN \cdot m^{-1}$
Density	7705	$kg \cdot m^{-3}$
Melting point	1683	K
Latent heat of solidification	67.46	$kJ \cdot g^{-1}$
Solidification interval	1683-1823	K

Fig. 4 shows the tip processing diagram of the bar, which is isometrically obtained from Fig. 1(b). It was assumed that the alloy bar melts from the edge of the cone after being heated by the super-frequency induction coil, and the droplets that flow down along the cone surface concentrate at the apex of the cone, forming a continuous flow.

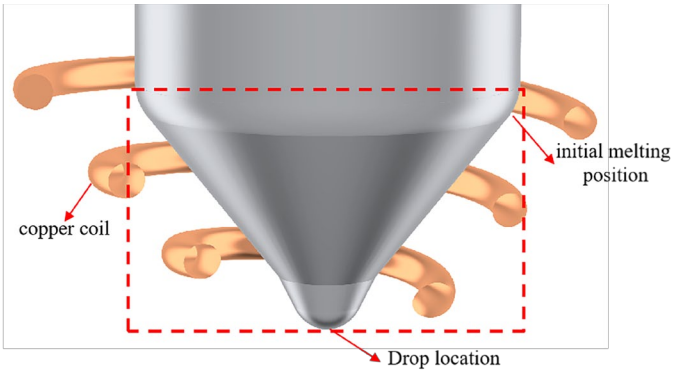

Fig. 4. Sharp conical melting head morphology of the superalloy electrode bar

To produce a continuous melting flow, the initial melting thickness of the bar was set as 0.4 mm after several simulation experiments. The model in Fig. 4 was developed by the AUTOCAD and GAMBIT software. Then, the model was meshed as shown in Fig. 5, where the number of meshes was about 35000, and the mesh density decreases gradually from the inlet (0.1 mm to 0.3 mm) for well converged simulations. Since the thickness of the melt inlet was 0.4 mm, a continuous fluid flow will be formed at the drop location after calculating for a certain time.

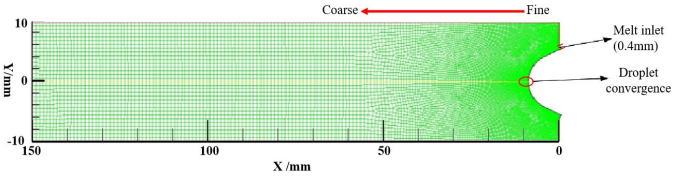

Fig. 5. Developed mesh of the superalloy electrode bar

The mesh file was imported into the FLUENT software, where a single-phase model was developed. The standard k-ε turbulence model was employed, and the applied metal parameters are listed in TABLE 2. The initial speed of the metal melt phase was 1.5 m/s. To obtain a converged and accurate solution, the scheme was set as SIMPLE for the solution method, the time step size was set as $6*10^{-7}$, and the number of time steps was 10^6. The process diagram is shown in Fig. 6.

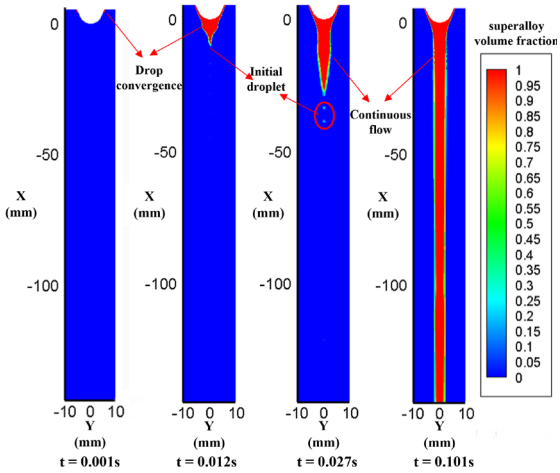

Fig. 6. Continuous metal melt flow

In Fig. 6, the droplets flow down along the surface and concentrate at the apex of the cone, and spheroidization and fracturing occur due to insufficient temperature of the initial droplet. Superheat of melting flow increases with smelting power, and melting droplets bond tighter and form a continuous flow, without any fracture. This condition can be regarded as the ideal situation in the EIGA process. Aly provided an Eulerian-Eulerian method of simulation for gas atomization, and the subsequent experiments on primary and secondary atomization were conducted on this basis [19].

2.3. Non-continuous metal melt flow simulation

Due to different actual production parameters, such as the number of turns, induction coil height, power, and operation process parameters, the flow of metal melt may exhibit a non-continuous state. The metal melt concentrated at the top of the metal bar converges into large droplets and flows until the surface tension is insufficient to balance gravity. Therefore, in the actual production process, the quality of the produced powder under discontinuous flow can be quite different than under continuous flow conditions [20].

To adequately simulate the melting process at the top of the metal bar, the same Ni-based superalloy bar as shown in Fig. 4 was employed. Supposing that the alloy bar melts from the edge of the cone after being heated by the super-frequency induction coil, the accumulated droplets gradually grow large until the surface tension is not sufficient to support them, leading eventually to the fall of the droplets. It was assumed that fluid droplets do not affect each other.

Based on previous experience of the actual production and multiple simulations, the initial melting thickness of the bar was set as 0.6 mm, ensuring that the flow will not be continuous during the simulation process. Using the same steps as in the simulation of continuous flow, the non-continuous melting process diagram is shown in Fig. 7.

As shown in Fig. 7, the formation of droplets can be divided into four stages, namely, elongation, necking, cracking, and spheroidizing. At the beginning stage of the elongation stage, the droplet is constantly elongated because the speed at the front of the droplet is higher than that at the opposite end. Then, due

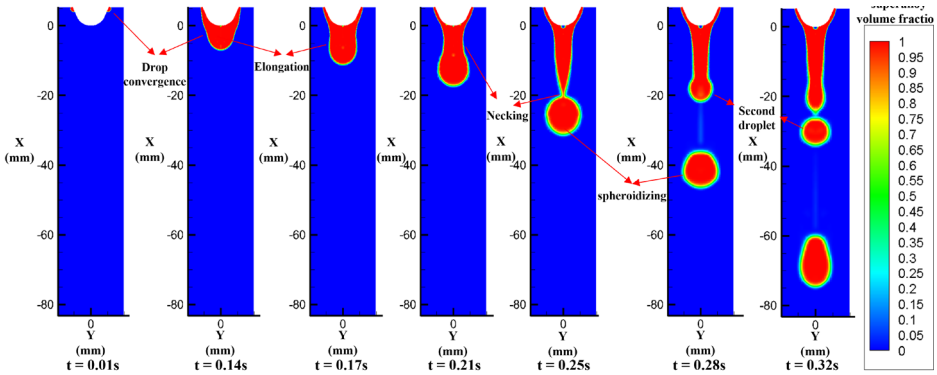

Fig. 7. Non-continuous metal melt flow

to adhesion on the bar surface, surface tension, and gravity, the front speed of the droplet gradually decreases, and the speed in the middle and at the tail gradually increases, while the fluid column continues to elongate. Along with the liquid flow on the surface of the bar which continuously forms liquid drops, a globular droplet begins to take on the shape of an ellipsoid, which is attributed to the increasing weight of the droplet. At that point, a neck region appears where the necking speed is higher than the front-end and tail speeds. As the speed increases, the necking region fractures, and a tail droplet is formed. Under the combined effect of air resistance, shear force, gravity, surface tension, and internal viscosity of the liquid, the tail of the droplet shrinks at the middle while, at the same time, vibration deformation of the ellipsoid droplet occurs in the air, which gradually breaks into a spherical droplet during the fall.

Fig. 7 supports the previous presumption that large droplets are present in the non-continuous melt flow process. By comparing Figs. 6 and 7, it can be intuitively deduced that the droplet diameter developed under continuous fluid flow is much smaller than that of the large droplet formed under non-continuous flow. Therefore, it can be speculated that in the actual production process, the phenomenon of fluid flow discontinuity may significantly affect the yield of high-quality powders.

3. Simulation of primary atomization

3.1. Parameter settings of primary atomization

A mesh model was developed by AUTOCAD and GAMBIT software, and, under the assumption that accuracy will not be affected, the model was simplified as a 2D model based on the symmetry of rotation to decrease the simulation workload (Fig. 8). It should be mentioned that the simulation was based on actual EIGA equipment nozzle drawings. The position of the air and metal fluid inlets were included in the model. To achieve better visualization of the flow and the atomization effect, the actual working range was reduced to the area within 200 mm below the nozzle.

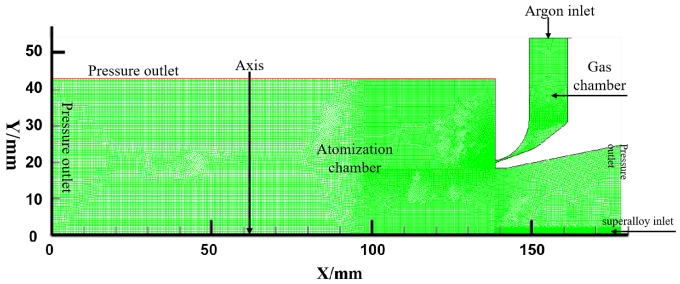

Fig. 8. Mesh model of the nozzle

The initial mesh density was varied to increase calculation accuracy, we designed three different grids to verify the independence of the mesh, the mesh numbers were 26119, 58410 and 154870, respectively. Then, the boundary conditions, such as axis, pressure inlet (gas), pressure outlet (gas), and velocity inlet (metal melt) were defined, and the 2D-mesh file was exported and imported into the FLUENT software, where the remaining parameters were set. Notably, the computational domain was 2D planar, which was not axisymmetric, and the shaft rotating axis in Fig. 8 was symmetry axis. To obtain better simulation results on the primary atomization process, the simulation of the stable single-phase air flow field (argon) was conducted first. The physical properties of argon are listed in TABLE 3. The *k-ε* turbulence model was again employed, the gas pressure was set as 4 MPa, the second order upwind scheme was selected from the possible schemes, the time step size was set as $6*10^{-7}$, and the number of time steps was 10^6. And we chose three points (0, 0; 80, 10; 125, 15) to observe the changes of the velocity in different grids, which was shown in Fig. 9.

TABLE 3

Physical properties of argon

Parameter	Value	Unit
Density	1.6228	$kg \cdot m^{-3}$
Cp (specific heat)	520.64	$J \cdot kg^{-1} \cdot k^{-1}$
Thermal Conductivity	0.0158	$W \cdot m^{-1} \cdot k^{-1}$
Viscosity	$2.125*10^{-5}$	$kg \cdot m^{-1} \cdot s^{-1}$
Molecular Weight	39.948	$kg \cdot kmol^{-1}$

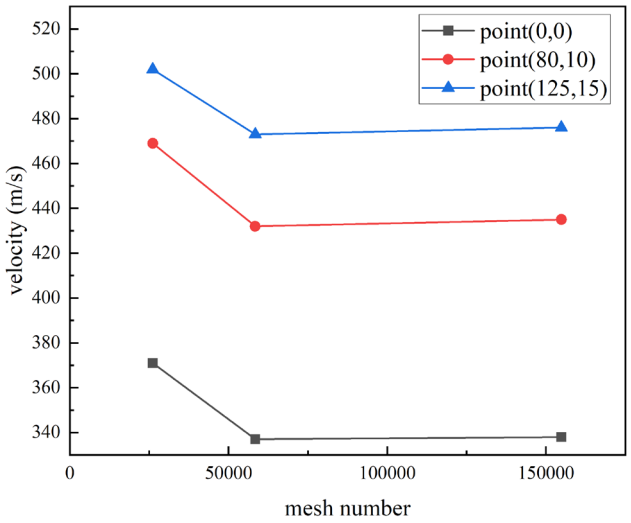

Fig. 9. Gas velocity under different model grid numbers

The velocity of three points was basically stable when the number of model grids had been increased from 58410 to 154870, so the number of grids 558410 for gas atomization simulation was independent. In this condition, the density around the nozzle area was high (about 0.1 mm) and lower in the other areas (about 0.5 mm), and the single-phase airflow field was shown in Fig. 10.

Based on the gas flow field, the volume of fluid (VOF) method and the large eddy simulation (LES) method were employed for both the continuous and non-continuous flow simulation. The physical properties of the used material are listed in TABLE 2, the initial velocity of the melt was 1.4 m/s and remained unchanged, and the temperature of the metal was 2000 K.

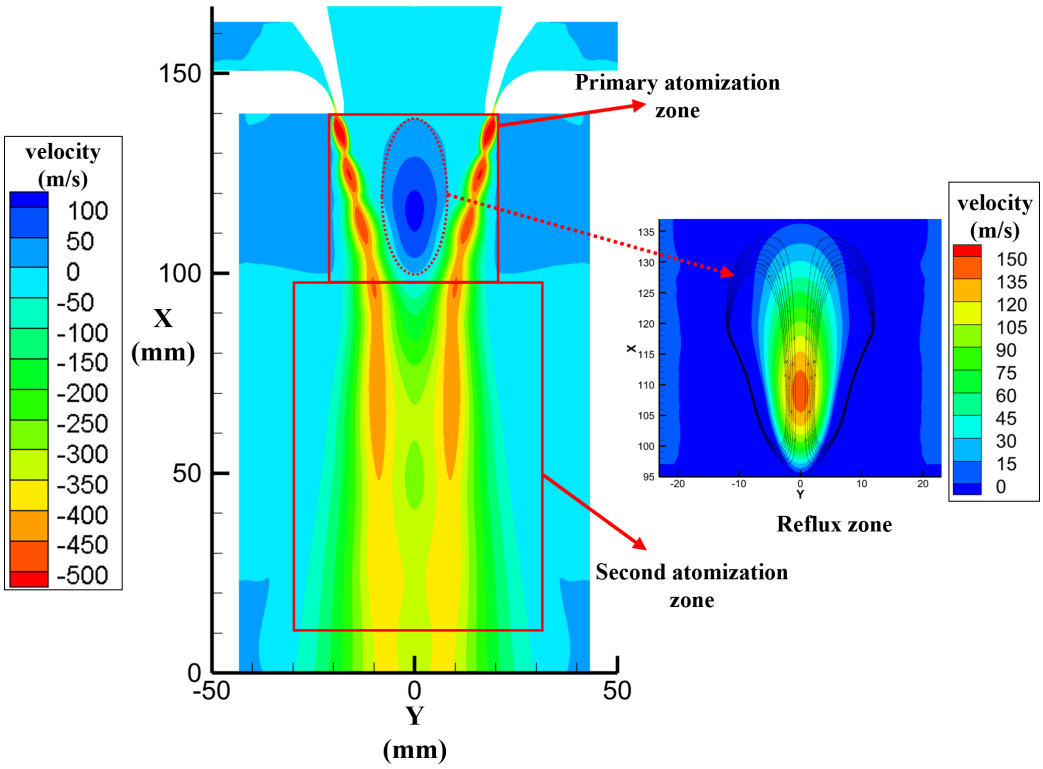

Fig. 10. Velocity vector field (m/s)

3.2. Simulation and comparison of primary atomization

As indicated in Fig. 6, the droplet diameter obtained in the continuous flow state was about 4 mm. For the droplet developed under non-continuous flow (Fig. 7), the drop time difference between the first drop and the second drop was established as 0.07 s, which is sufficient for primary atomization. Hence, it can be assumed that there is no mutual force between large droplets, and the calculation result is not affected if only one large droplet is imported.

After a period of calculation, primary atomization occurred when the position of the metal fluid flow and the nozzle position were in the same horizontal line (Fig. 11), at the top of the reflux zone. The metal fluid flow is affected by the high-speed argon flow, where strong thermal and kinetic energy exchange occurs, and the melt gradually breaks into tiny melt droplets.

In Fig. 11, the droplet diameter developed under continuous and discontinuous fluid flow was different, which directly affected the crushing effect during the primary atomization process. One can observe the continuous metal flow just above

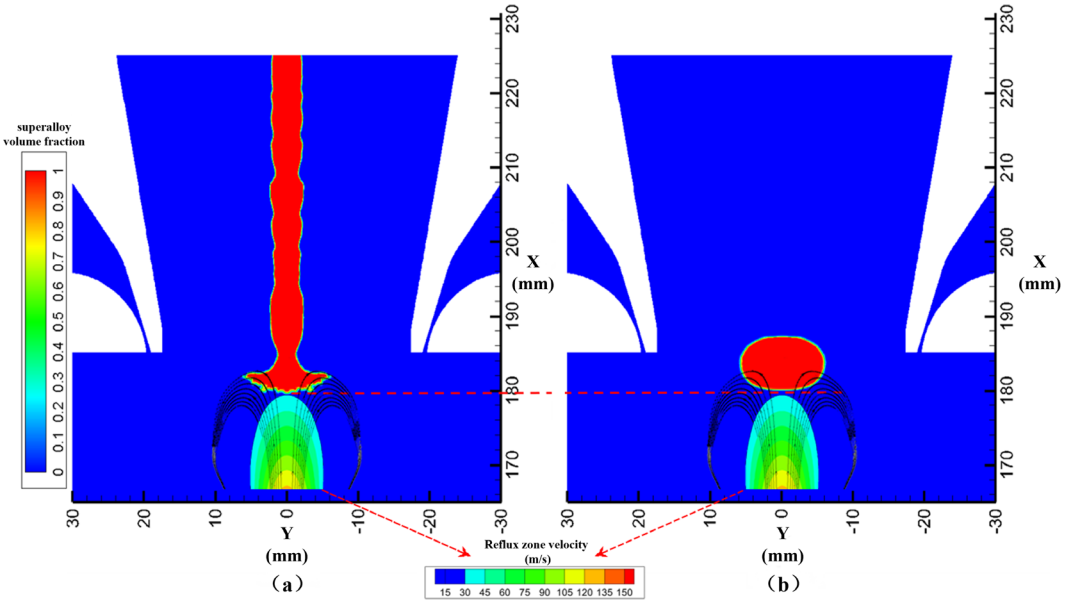

Fig. 11. Metal melt flow; (a) Continuous flow, t = 0.0389 s (b) non-continuous flow, t = 0.0263 s

the recirculation zone, indicating the possible impact of the metal flow by the largest velocity of the reflux zone and the occurrence of a complete exchange of kinetic and thermal energy in the process. Only a part of the non-continuous metal flow can have a direct collision and energy exchange with the reflux area, which will result in incomplete fragmentation.

According to the references on Rayleigh instability [21,22], a surface tension-driven process is the main physical mechanism responsible for the break-up of a thin liquid metal stream into smaller droplets, which can be described by:

$$\lambda = \sqrt{2}\pi D\sqrt{1+3\mu\left(\rho\gamma D\right)^{-1/2}} \tag{1}$$

$$\lambda_* = \pi D/\chi_* \tag{2}$$

where λ is wavelengths of the liquid; D is the diameter of the liquid; μ, ρ, and γ are the viscosity, surface tension, and the density of the superalloy, respectively; $\chi_* = 1.0668$. The liquid becomes more unstable as λ/λ_* increases, which can be defined as:

$$\frac{\lambda}{\lambda_*} = \frac{\sqrt{2\left(1+3\mu\left(\rho\gamma D\right)^{-1/2}\right)}}{\chi_*} \tag{3}$$

The value of λ/λ_* decreases with the increase in D, which explains why thinner liquid streams break-up into smaller droplets. Therefore, after the primary atomization of the continuous fluid, the droplet size is smaller, which is related to the initial state of the fluid flow.

To observe smaller droplets and achieve better accuracy of the simulation results, the mesh needs to be encrypted to the million-level before the metal flow contacts the high-speed gas. Then, a specific range or fluid phase was selected to refine the mesh on the Adaptation Controls interface until the number of grids increases to 866736 and the boundary of atomized droplets was captured. Subsequently, the data file generated by FLUENT was imported into the post-processing software TECPLOT for analysis, where the scale bar was adjusted, the metal phase was selected in the contour settings, and the X-axis and Y-axis ranges were set from 160 to 225 mm and from –30 to 30 mm, respectively. Fig. 12 was obtained after adjusting the display ruler, the display area, the position, and the drop-shaped profile map.

In Fig. 12, the metal melt fluid comes into contact with the high-speed gas at a position parallel to the nozzle; Xia named this phenomenon “umbrella break-up” [12], which was the primary atomization. To assess the model validity, the total metal mass before the primary atomization and after the breakup occurred was calculated in TABLE 4.

For the data in TABLE 4, the continuous falling of the melt during the atomization process was considered in the calculation of the mass change rate. The calculated change rates were 0.81% and 0.25%, which verified the mass conservation of the model.

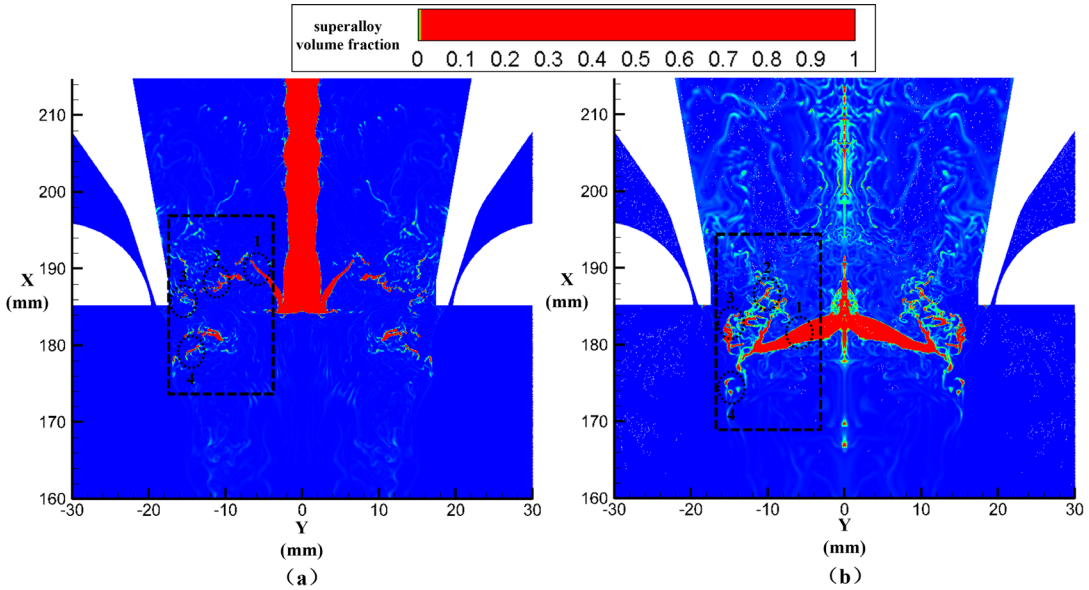

Fig. 12. Comparison of droplet topography; (a) Primary atomization of continuous metal melt, t = 0.0425 s, (b) Primary atomization of non-continuous metal melt, t = 0.0297 s

TABLE 4

Metal mass before and after primary atomization

Melt state	The metal mass (kg)		Atomization time (s)	Increased mass (kg)	Change rate
	before breakup	after breakup			
Continuous	0.00476979	0.00485530	$1*10^{-3}$	0.00012413	0.81%
Non-continuous	0.00410748	0.00409739	$1*10^{-3}$	0	0.25%

When comparing Figs. 12(a) and (b), the fragmentation degree of the droplet in Fig. 12(a) was much greater than that in Fig. 12(b).

The primary atomization droplet is indicated as the circled part in Fig. 12. According to the simulation data, the temperatures of the identification points in Fig. 12 can be obtained, which are listed in TABLE 5.

Based on the data in TABLE 5, the temperature drop of continuous liquid flow after impact through the reflux zone is not clear, whereby the temperatures are all above 1900 K and far above melting temperature. While the temperature drop is much larger for non-continuous than for continuous liquid flow, points 2 and 4 in Fig. 12(b) are below 1550 K, which indicates that these droplets have solidified without secondary atomization, resulting in the generation of large-size particles and even satellite particles.

The large volume of the metal droplets developed under non-continuous flow results in a reduced contact area with the high-speed airflow, causing insufficient exchange of kinetic energy and heat. Thus, the volume of droplets generated under non-continuous primary atomization is larger than those obtained under continuous primary atomization. The result of the primary atomization is the basis for the secondary atomization. From Fig. 12, it can be inferred that the particle size obtained by discontinuous fluid flow is larger than that obtained by continuous fluid flow. This will be verified in the simulation of secondary atomization.

The melt volume fraction was lowered in the TECPLOT software by selecting the continuous color map distribution method and adjusting the contour values at endpoints, which demonstrates the original appearance of most droplets and increases the accuracy of the secondary atomization simulation. The continuous primary atomization results were selected in Fig. 13.

The droplet area shown in Fig. 13 is the original appearance after primary atomization. The shape of the droplets is irregular and most of them resemble long curved strips. The "bag-breakup" mechanism can be presumed as the crushing mechanism. The process is similar to the burst of soap bubbles blown out of a soap film. In particular, the thin hollow packet eventually bursts to form many small pieces, the edges of which merge into a smaller number of large pieces. The circled droplet in Fig. 13(a) is much smaller than that in Fig. 13(b), which also verifies that the primary atomization under continuous flow is better than that under non-continuous flow.

Since the crushing process of the metal melt was not entirely completed after primary atomization, a numerical simulation of secondary atomization is required. Fig. 13 was used as the data basis for the secondary atomization. It should be mentioned that continuous and non-continuous fluid flow were treated the same.

4. Simulation of secondary atomization

According to reference [12], the completely broken droplets under the nozzle were chosen as the initial droplets for the secondary atomization simulation (Fig. 13), and the cross section of the droplets was fitted into a sphere of the same volume before determining the distribution of the diameter.

TABLE 5

Temperatures of partial primary droplets in Fig. 12

Points	Fig. 12(a)				Fig. 12(b)			
	1	2	3	4	1	2	3	4
Temperature /k	1997	1981	1955	1947	1911	1519	1688	1126

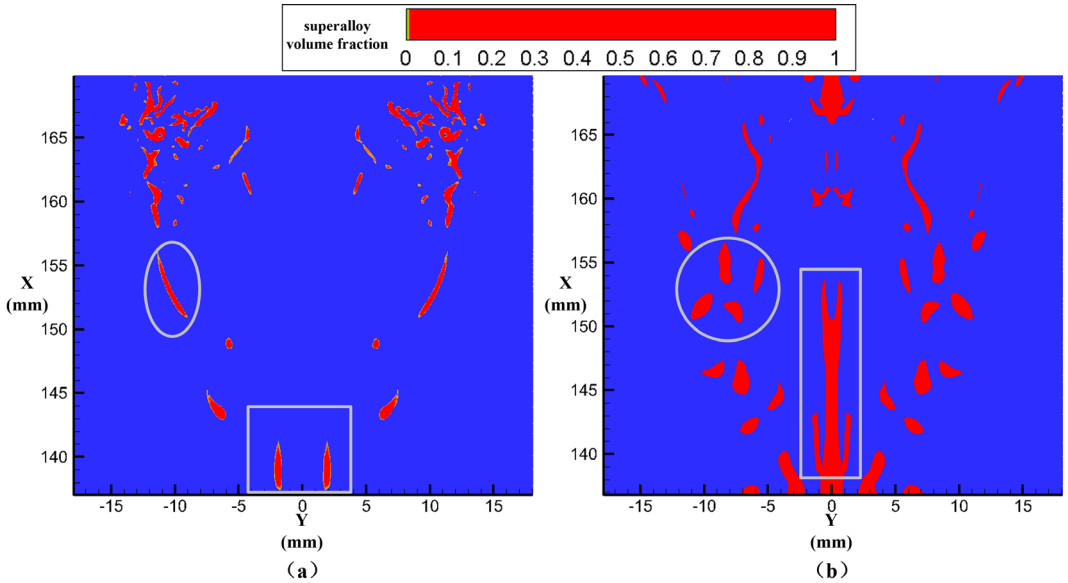

Fig. 13. Droplets of metal melt in primary atomization; (a) Continuous metal melt, (b) non-continuous metal melt

In general, in two-phase flow processes, several functional distribution methods are usually employed when discrete phase models (DPMs) are used to simulate two-phase flows. The most common formulas are the linear distribution and the Rosin-Rammler distribution. In this paper, the following formula was used:

$$n = \frac{\ln\left(-\ln Y_d\right)}{\ln d/\bar{d}} \tag{4}$$

where n is the Rosin-Rammler uniformity index (a smaller n value indicates a wider particle size distribution range), Y_d is the proportion of particle size distribution, and d and $\bar{d}$ are the size distribution parameters in the Rosin-Rammler equation. The n values of continuous and non-continuous fluid flow were calculated as 1.2945 and 1.0584, respectively, which indicates the narrower particle size distribution obtained with continuous fluid flow.

The aerodynamic coefficients Weber number (*We*) and Ohnesorge number (*Oh*) are important dimensionless parameters in secondary atomization. *We* is the ratio of turbulence aerodynamic force and relative surface tension, while Oh represents the ratio of viscosity to surface tension. A large *We* indicates stronger splintering tendency, while a large *Oh* indicates lower splintering tendency. With the increase in *We*, a variety of typical secondary crushing patterns, including Taylor Analogy Breakup (TAB) models, Wave models, and Kelvin-Helmholtz (KH) models, appears [23].

We can be defined as:

$$We = \frac{\rho_g U^2 d_L}{\sigma} \tag{5}$$

where ρ_g is the gas density, U is the relative velocity of the gas and the slow-moving droplet, d_L is the droplet diameter after primary atomization, and σ is the surface tension of the molten droplet.

Oh can be defined as:

$$Oh = \frac{\mu_d}{\sqrt{\rho_d d_d \sigma}} \tag{6}$$

where μ_d is the viscosity of the melt droplet, ρ_d is the density of the droplet, σ is the surface tension of the molten droplet, and d_d is the droplet diameter after primary atomization.

4.1. Parameter setting of secondary atomization

Based on the primary atomization results presented in section 3.2 (Fig. 13), the parameters ρ_{Ar}, U, d_L, and σ can be obtained. Then, *We* was calculated as ranging from 23 to 95, which determines that the TAB model should be selected [24].

The simulation of secondary atomization was performed based on the single-phase gas field (Fig. 10) and the primary atomization simulation (Fig. 13). The standard k-ε turbulence model and the DPM, which can reflect the mutual effect between gas and droplets during atomization, were employed. Then, the DPM model was set to load particles in the range where the main atomization occurs. The physical parameters of the metal particles were the same as in Table 2. In addition, the mass flow rate was set as 0.04 kg/s based on the gas flow, the diameter parameters conformed to the Rosin-Rammler distribution, and the particle size of the droplets at the outlet were monitored until the secondary atomization calculation was completed.

4.2. Simulation process and analysis of secondary atomization

Based on the visualization of the FLUENT software, the trajectory of the secondary atomized metal particles under continuous and discontinuous flow was obtained (Fig. 14).

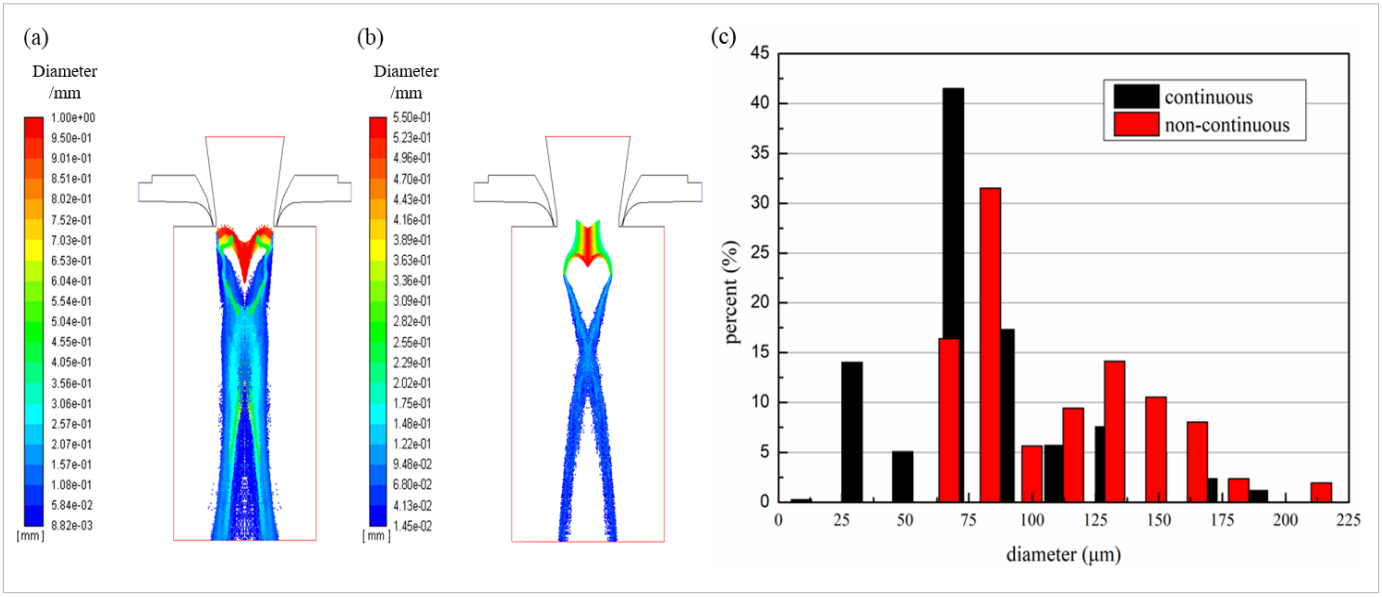

Fig. 14 Diameter distribution in secondary atomization; (a) Continuous metal melt, (b) non-continuous metal melt, (c) diameter distribution

According to the trajectory of the secondary atomization in Fig. 14, the large droplets produced by the primary atomization were further broken into smaller droplets. The impact of high-speed airflow caused the two metal droplets to flow along with the gas, which then crushed further and solidified into metal powders. Comparing Figs. 14(a) and (b) reveals that the particles developed under non-continuous secondary atomization were much larger than those obtained under continuous fluid flow. Due to the faster cooling of the liquid during the discontinuous fluid flow, the particle size of secondary atomization at the middle of the jets was basically unchanged and remained distributed in a large range. The crushing effect was far less than that in the secondary atomization under continuous fluid flow.

To compare the effect of the two types of fluid atomization more intuitively, the statistical parameters of the escaped particles was set before the beginning of the calculation. The particle size distribution obtained for both cases is presented in Fig. 14(c).

Based on the simulation results in Fig. 14(c), the diameter distribution of the powders obtained from continuous fluid flow can be determined. The D50 size was about 70 μm, which was consistent with the particle size distribution of the powder particles obtained in the actual production process. Furthermore, the D50 size of the non-continuous atomized powders was about 100 μm, a small number of large particle powders with a diameter of at least 150 μm were present, and the quality of the powders was far lower than that of the continuous atomized powders. The results of the numerical simulation agreed well with the experimental measurements described in Fig. 3.

Through the secondary atomization simulation, the core idea put forward in sections 2 and 3 has been finally verified: the quality of powders obtained under continuous fluid atomization is better than that obtained under non-continuous atomization. The simulation results were in good agreement with the experimental results (Fig. 2) obtained in the actual production process.

It can be concluded that the non-continuous melt flow produces larger droplets, which can be attributed to the melting rate, surface tension, and other parameters. The simulation of the metal melt flow and the simulation of the primary atomization process reveal that the non-continuous fluid flow does not break up sufficiently due to the lack of kinetic energy and heat exchange. In addition, the simulation of secondary atomization verified directly from the data that the powder quality obtained under non-continuous fluid flow conditions was lower than that obtained from continuous fluid flow.

5. Conclusions

This work performed CFD numerical simulations to investigate the flow of metal melt during EIGA. The flow of molten superalloy and the primary atomization process were numerically simulated using single-phase flow and multi-phase flow models, and the difference between continuous and discontinuous liquid flow was observed intuitively. The droplet size of the primary atomization during continuous liquid flow was much smaller than that obtained with non-continuous flow, which was caused by Rayleigh instability. The primary atomization crushing results were used as the initial condition in the secondary atomization simulation. The secondary atomization splits the initially broken large droplets of the melt into finer droplets. The process was calculated using the TAB model, and the particle size distribution was calculated by monitoring the escaped particles.

According to the actual production and numerical simulation results, the D50 particle size of powder prepared by atomization under continuous liquid metal flow was about 70 μm, while that obtained by atomization under non-continuous liquid metal flow was about 100 μm. The diameter distribution results of the numerical simulations agreed well with the experimental measurements, and the necessity and significance of ensuring continuous fluid flow in the EIGA process were verified. Furthermore, the theoretical and computational basis for achieving continuous liquid flow was provided, as well as guidance for improving the production process of fine powders using EIGA.

REFERENCES

[1] H. Zhu, H. Tong, F. Yang, C. Cheng, Plasma-assisted preparation and characterization of spherical stainless steel powders, Journal of Materials Processing Technology **252**, 559-566 (2018).

[2] C.-R. Si, X.-J. Zhang, J.-B. Wang, Y.-J. Li, Design and evaluation of a Laval-type supersonic atomizer for low-pressure gas atomization of molten metals, International Journal of Minerals, Metallurgy, and Materials **21** (6), 627-635 (2014).

[3] V.C. Srivastava, S.N. Ojha, Effect of aspiration and gas-melt configuration in close coupled nozzle on powder productivity, Powder Metallurgy **49** (3), 213-218 (2013).

[4] C.L. Qiu, M.M. Attallah, X.H. Wu, P. Andrews, Influence of hot isostatic pressing temperature on microstructure and tensile properties of a nickel-based superalloy powder, Materials Science and Engineering: A **564**, 176-185 (2013).

[5] V. Bojarevics, F. Dughiero, A. Roy, K. Pericleous, Numerical model of electrode induction melting for gas atomization, COMPEL - The international Journal For Computation and Mathematics in Electrical and Electronic Engineering **30** (5), 1455-1466 (2011).

[6] M. Zheng, S. Zhang, Q. Hu, J. Xu, W. Mao, L. Lu, H. He, Y. Liu, W. Zhao, A novel crucible-less inert gas atomisation method of producing titanium powder for additive manufacturing, Powder Metallurgy **62** (1), 15-21 (2018).

[7] M. Hohmann, N. Ludwig, Einrichtung zum Herstellen von Pulvern aus Metallen, 1991.

[8] S. Özbilen, A. Ünal, T. Sheppard, Influence of Liquid Metal Properties on Particle Size of Inert Gas Atomised Powders, Powder Metallurgy **39** (1), 44-52 (2013).

[9 J. Ting, I.E. Anderson, A computational fluid dynamics (CFD) investigation of the wake closure phenomenon, Materials Science and Engineering: A **379** (1-2), 264-276 (2004).

[10] M. Wei, S. Chen, J. Liang, C. Liu, Effect of atomization pressure on the breakup of TA15 titanium alloy powder prepared by EIGA method for laser 3D printing, Vacuum **143**, 185-194 (2017).

[11] K.-K. Guo, C.-S. Liu, S.-Y. Chen, H.-H. Dong, S.-Y. Wang, High pressure EIGA preparation and 3D printing capability of Ti-6Al-4V powder, Transactions of Nonferrous Metals Society of China **30** (1), 147-159 (2020).

[12] M. Xia, P. Wang, X. Zhang, C. Ge, A computational fluid dynamics (CFD) investigation of the primary and secondary atomization of the free-fall atomizer in EIGA process, Act Physica Sinica-Chinese Edition **67**, 41-51 (2018).

[13] Y. Minghao, W. Rui, L. Kai, Y. Jiafeng, Numerical simulation of three-dimensional transient flow characteristics for a dual-fluid atomizer, Engineering Applications of Computational Fluid Mechanics **13** (1), 1144-1152 (2019).

[14] S. Motaman, A.M. Mullis, R.F. Cochrane, I.N. McCarthy, D.J. Borman, Numerical and experimental modelling of back stream flow during close-coupled gas atomization, Computers & Fluids **88**, 1-10 (2013).

[15] N. Zeoli, S. Gu, Numerical modelling of droplet break-up for gas atomisation, Computational Materials Science **38** (2), 282-292 (2006).

[16] X. Chen, Study on the flow field structure and atomization mechanism of close coupled gas atomization, Central South University, 2007, p. 97.

[17] S. Feng, M. Xia, C.-C. Ge, Consecutive induction melting of nickel-based superalloy in electrode induction gas atomization, Chinese Physics B **26** (6), (2017).

[18] J. Ting, J. Connor, S. Ridder, High-speed cinematography of gas-metal atomization, Materials Science and Engineering: A **390** (1-2), 452-460 (2005).

[19] H.S. Aly, Y.A. Eldrainy, K.M. Saqr, T.M. Lazim, M.N.M. Jaafar, A mathematical model for predicting spray atomization characteristics in an Eulerian-Eulerian framework, International Communications in Heat and Mass Transfer **37** (6), 618-623 (2010).

[20] R. Kaiser, C. Li, S. Yang, D. Lee, A numerical simulation study of the path-resolved breakup behaviors of molten metal in high-pressure gas atomization: With emphasis on the role of shock waves in the gas/molten metal interaction, Advanced Powder Technology **29** (3), 623-630 (2018).

[21] S. Chandrasekar, Hydrodynamic and Hydromagnetic Stability, Dover, New York, 1981.

[22] S. Spitans, H. Franz, E. Baake, Numerical Modeling and Optimization of Electrode Induction Melting for Inert Gas Atomization (EIGA), Metallurgical and Materials Transactions B **51** (5), 1918-1927 (2020).

[23] I. ANSYS, ANSYS Fluent Users Guide, 2181-2354 (2020).

[24] N. Zeoli, H. Tabbara, S. Gu, CFD modeling of primary breakup during metal powder atomization, Chemical Engineering Science **66** (24), 6498-6504 (2011).